Research Square

Preprints are preliminary reports that have not undergone peer review.
They should not be considered conclusive, used to inform clinical practice,
or referenced by the media as validated information.

Immune Inflammation in Brown Adipose Tissue and Altered Lipid Metabolism in the Liver Under Geomagnetic Field Shielding

Xuejing Ma

buddyma@163.com

Cangzhou Normal University

Dunqin Gao

Chinese Academy of Medical Science & Peking Union Medical College

Guanqun Kou

Cangzhou Normal University

Wenya Xu

Cangzhou Normal University

Jiaxuan Zhao

Cangzhou Normal University

Huili Wang

Cangzhou Normal University

Songyuan Duan

Cangzhou Normal University

Jingyi Zhang

Cangzhou Normal University

Ruoxi Zhang

Cangzhou Normal University

Xinyi Jiang

Cangzhou Normal University

Short Report

Keywords:

Posted Date: November 6th, 2026

DOI: https://doi.org/10.21203/rs.3.rs-11622408/v1

License: This work is licensed under a Creative Commons Attribution 4.0 International License.
Read Full License

Additional Declarations:
No competing interests reported.

All experimental procedures involving animals were approved by the Animal Ethical and Welfare Committee of Cell Ecology Haihe Laboratory (Approval No: HH-DWLL-YW2025009-1).

Immune Inflammation in Brown Adipose Tissue and Altered Lipid Metabolism in the Liver Under Geomagnetic Field Shielding

Xuejing Ma[1#*], Dunqin Gao[2#], Guanqun Kou[1], Wenya Xu[1], Jiaxuan Zhao[1], Huili Wang[1], Songyuan Duan[1], Jingyi Zhang[1], Ruoxi Zhang[1], Xinyi Jiang[1]

[*]Correspondence: Xuejing Ma, buddyma@163.com

Dunqin Gao, gaodunqin@163.com

Guanqun Kou, hebtu10100@qq.com

Wenya Xu, xuwenya@cau.edu.cn

Jiaxuan Zhao, 3137851435@qq.com

Huili Wang, 3150969276@qq.com

Songyuan Duan, 2422907596@qq.com

Jingyi Zhang, 2406841375@qq.com

Ruoxi Zhang, zhangruoxi0729@163.com

Xinyi Jiang, 778364434@qq.com

[#]These authors contributed equally to this work.

[1]Department of Life Sciences, Hebei Key Laboratory of Bohai Rim Biomass Materials, Cangzhou Normal University, Cangzhou 061000, Hebei, China

[2]State Key Laboratory of Advanced Medical Materials and Devices, Engineering Research Center of Pulmonary and Critical Care Medicine Technology and Device (Ministry of Education), Institute of Biomedical Engineering, Tianjin Institutes of Health Science, Chinese Academy of Medical Science & Peking Union Medical College, Tianjin 300192, China

Abstract

Objective Hypomagnetic field is an environmental factor in deep space that affect multiple systems in human body, but how they impact the immunometabolism of metabolic tissues such as brown adipose tissue (BAT) and liver is still unclear. This study used geomagnetic shielding (GS) environment to simulate hypomagnetic field and preliminarily explored its effects on BAT and liver immunometabolism.
Results GS environment caused different immunometabolic changes in BAT and liver. In BAT, the GS environment was associated with immune inflammatory pathways and also affected glucose and lipid metabolism as well as autophagy related to lipid droplets (LDs). Transferrin receptors were enriched on LDs in both GS and non-GS conditions. In liver, GS environment was linked to lipid metabolic pathways such as cholesterol, fatty acid, and glycerophospholipid metabolism, and innate immune responses related to antiviral defense were also activated. Fatty acid synthase was upregulated at both transcriptomic and LD proteomic levels. Furthermore, TAG accumulated significantly in hepatic LDs under GS conditions. These results suggest that GS environment leads to tissue-specific immunometabolic changes in BAT and liver, providing a theoretical basis for developing health protection strategies for astronauts.
Keywords geomagnetic shielding, brown adipose tissue, liver, lipid droplet, immunometabolism

Introduction

The geomagnetic field (GMF) is essential for life(1, 2). The hypomagnetic field (HMF, <5 μT), prevalent in deep space(3, 4), disrupts neurogenesis and early embryonic development(5, 6), and is linked to altered cell proliferation, nervous system function, oxidative stress, DNA integrity, microbiome, and infection risk(7). HMF affects intracellular reactive oxygen species (ROS), with mitochondria regulating metabolism and ROS production(8). However, its impact on brown adipose tissue (BAT) and liver remains unclear.
HMF regulates glycogen synthase kinase-3 beta (GSK-3β) and mammalian target of rapamycin (mTOR) phosphorylation, impacting neural stem cell proliferation(9); exacerbates bone loss and iron metabolism disorders(10-12); elevates ROS and impairs mitochondrial function(8, 13); promotes anaerobic glycolysis(14); inhibits respiratory chain complex I(15); and reduces skeletal muscle mitochondrial activity and exercise capacity(16). Early studies showed 100-fold weakened GMF increases lipid peroxidation, reduces antioxidant enzymes, and alters plasma lipids in guinea pigs and rats(17). Repeated strong static magnetic fields inhibit rat liver synthesis(18). HMF affects immunity in rats in a gender-dependent manner, with delayed thymus degeneration, increased peritoneal macrophages, and reduced nitric oxide (NO) and superoxide anion production(19); in *Caenorhabditis elegans* (*C. elegans*), increased stress response and lifespan but reduced reproduction and size(20); decreased neutrophil ROS via nicotinamide adenine dinucleotide phosphate (NADPH) oxidase, disrupted by mitochondrial uncouplers(21). However, tissue-specific immunometabolism in BAT and liver is unstudied.
Immunity is integral to metabolic regulation. BAT thermogenesis relies on local immune homeostasis maintained by heterogeneous regulatory T cells (Tregs), whose depletion releases interferon-gamma (IFN-γ)-producing lymphocytes, causing mitochondrial dysfunction and blocking non-shivering thermogenesis, while cold expands interleukin-18 receptor 1 (IL-18R1)+ Tregs(22). Immune microenvironment determines fatty liver pathogenesis(23, 24). Thus, HMF effects on BAT and liver immunometabolism are essential for space metabolic risk assessment. No studies have linked HMF to BAT and liver immune metabolism.
In this study, geomagnetic shielding (GS) environment refers to housing mice in a magnetically shielded cage to attenuate ambient GMF. We integrated transcriptomics with LD proteomics to investigate tissue-specific effects. We examined whether the GS environment is associated with immune and metabolic changes in both BAT and the liver. Our findings provide a foundation for astronaut protection and for treating obesity, diabetes, and fatty liver.

Materials and methods

Geomagnetic Shielding Environment

The geomagnetic shielding environment was created using tri-axial Helmholtz coil systems, as previously described(25). Mice were kept in the geomagnetic shielding environment or in the same system operated identically with the power off. According to regional geomagnetic data, the local geomagnetic field ranged between (54218.75-17.8) nT and (54218.75+33.3) nT (Fig. S5). The residual

magnetic field inside the shielding device, based on prior measurements(25), is estimated to be slightly below 0.17 μT.

Animals

Adult male C57BL/6J mice (8-10 weeks old) were purchased from Beijing Vital River Laboratory Animal Technology Co., Ltd. Mice were randomly divided into a non-shielded control group and a GS group (n = 3 per group) and group-housed under standard conditions (22 ± 1°C, 65 ± 1% humidity, 12 h reverse light-dark cycle with lights on at 08:00 and off at 20:00), with standard chow and filtered water ad libitum. After 4 weeks of treatment (24 h/day), mice were euthanized by cervical dislocation for collection of liver and BAT.

Lipid droplet purification

Liver tissues were rinsed with ice-cold phosphate-buffered saline (PBS) (140 mM NaCl, 2.7 mM KCl, 10 mM $Na_2HPO_4{\cdot}12H_2O$, 1.8 mM KH_2PO_4, pH 7.4). A portion was snap-frozen in TRIzol for transcriptomics; the remainder was homogenized in Buffer A (250 mM sucrose, 25 mM Tricine, pH 7.8). After centrifugation at 500 g to remove debris, the supernatant was carefully overlaid with Buffer B (20 mM 4-(2-hydroxyethyl)-1-piperazineethanesulfonic acid (HEPES), 100 mM KCl, 2 mM $MgCl_2$, pH 7.4) and subjected to gradient centrifugation (2,000 g, 4,000 g, and 8,000 g, 20 min each) to collect LD fractions(26). For BAT, one portion was used for transcriptomics, and the remainder was homogenized and subjected to differential centrifugation (500 g, 2,000 g, and 8,000 g, 5 min each) for LD isolation. The 8,000 g pellet was washed three times and resuspended in 400 μL Buffer B to yield the rough mitochondria (MT) fraction(27). LDs isolated from the same tissue of an individual mouse at different speeds were pooled. The pooled BAT LDs and the MT fractions were defatted with chloroform: acetone (3:1), and stored at −80°C for proteomics, or solubilized in 2×SDS sample buffer, denatured at 95°C for 5 min, and used for silver staining and immunoblotting.

Transcriptomic and proteomic analysis

Biological replicates (n = 3 per group) were processed individually. Total RNA was extracted from individual mouse tissues using TRIzol. For mRNA library construction, 1 μg of total RNA per sample was used for poly(A) enrichment via Oligo(dT) beads, followed by fragmentation and random-primed cDNA synthesis. After end repair, dA-tailing, adaptor ligation, and PCR amplification, the libraries were sequenced on Illumina NovaSeq or MGI2000 platforms using a 2×150 paired-end (PE) configuration. Reads were aligned to GRCm39 (Ensembl v107) with HISAT2 (v2.2.1) and quantified with HTseq (v0.6.1). For LD proteomics, LD proteins from each mouse were processed independently; tryptic peptides were separated by nanoflow LC and analyzed by data-independent acquisition (DIA) on a timsTOF Pro2. Raw data were searched against the UniProt mouse database (2023-09) using SpectroMine (v4.2) with 1% false discovery rate (FDR).

Bioinformatic analyses were performed in R. Differential expression was analyzed with DESeq2 (transcriptome) and t-test (LD proteome), using $|\log_2 FC| > 0.59$; these models jointly analyze all replicates to estimate a single $\log_2$ fold change ($\log_2 FC$) and P-value, accounting for variance among the three biological replicates. Kyoto Encyclopedia of Genes and Genomes (KEGG) enrichment used clusterProfiler, and integrated results were visualized with Sankey diagrams. $P < 0.05$ was considered significant.

For long non-coding RNA (lncRNA) identification, transcripts overlapping known protein-coding genes, microRNAs (miRNAs), transfer RNAs (tRNAs), small nucleolar RNAs (snoRNAs), ribosomal RNAs (rRNAs), or pseudogenes (UCSC, Ensembl, GENCODE) were filtered out. Remaining transcripts were retained if ≥200 bp, ≥2 exons, and ≥3 supporting reads. Transcripts with protein domains (HMMER-3, E-value ≤ 1e-5, Pfam) or protein-coding potential (coding potential calculator, CPC) were removed.

Lipid composition analysis

Lipid composition of isolated LDs was analyzed by thin-layer chromatography (TLC) and enzymatic quantification. For TLC, the organic phase from LD protein extraction was dried under nitrogen, resuspended in 100 μL chloroform, and spotted onto silica gel plates (Merck). Triolein (Sangon Biotech) and soybean- and egg-derived lecithin (Sangon Biotech) served as triacylglycerol (TAG) and phospholipid markers, respectively. Plates were developed in chloroform: methanol: acetic acid: water (75:13:9:3, v/v/v/v), and lipids were visualized by iodine vapor. Phosphatidylcholine (PC) bands were quantified by densitometry using ImageJ (NIH). For TAG quantification, dried lipids were dissolved in isopropanol and assayed with an Amplex Red Triglyceride Assay Kit (Beyotime); absorbance was measured at 570 nm,

and TAG concentrations were normalized to LD protein content measured by bicinchoninic acid assay (BCA).

Real-time quantitative PCR

Total RNA was reverse-transcribed using the HiScript 1st Strand complementary DNA (cDNA) Synthesis Kit. Quantitative polymerase chain reaction (qPCR) was performed with AceQ qPCR SYBR Green Master Mix (without ROX), with three technical replicates per sample, on a Bio-Rad CFX96 or ABI QuantStudio instrument. Primers were designed using Primer Premier 6 and Oligo 7.37, synthesized by Beyotime Biotechnology, and are listed in Table S1. Actin beta (ACTB) served as the internal reference, and relative expression was calculated using the $2^{-\Delta\Delta Ct}$ method.

Protein analysis by silver staining and Western blot

Protein samples from isolated LDs and subcellular fractions (whole cell lysate (WCL), post-nuclear supernatant (PNS), cytosol (CYTO), and total membrane (TM)) were analyzed. For silver staining, proteins were separated by sodium dodecyl sulfate-polyacrylamide gel electrophoresis (SDS-PAGE) (Beyotime) and stained with a silver staining kit (Beyotime) according to the manufacturer's instructions. For Western blot, proteins were transferred to polyvinylidene fluoride (PVDF) membranes, blocked with 5% non-fat milk in Tris-buffered saline with Tween 20 (TBST), and incubated overnight at 4°C with primary antibodies against adipose triglyceride lipase (ATGL), transferrin receptor (TFR1), fatty acid synthase (FASN) or glyceraldehyde-3-phosphate dehydrogenase (GAPDH) (1:1000, Cell Signaling Technology). After washing, membranes were incubated with horseradish peroxidase (HRP)-conjugated secondary antibodies (1:1000, Beyotime) and visualized using BeyoECL Star chemiluminescent substrate (Beyotime).

Determination of total iron in cytosol

BAT and liver cytosol samples were mixed with 5 μL 1 M HCl per 100 μL, incubated at 60°C for 30 min, and centrifuged at 12,000 g at 4°C for 10 min. The supernatant was collected for total iron detection using an iron detection kit (Beyotime) with a 0-50 μM Iron Standard curve. In a 96-well plate, blank, standard, and sample wells were set up. Sample wells received 30 μL supernatant, 20 μL Reduction Buffer, and 5 μL Decontamination Solution; the volume was brought to 190 μL with Assay Buffer and incubated at 37°C for 30 min. Then 10 μL Iron Probe was added, mixed, and incubated in the dark at 37°C for 30 min. Absorbance was measured at 593 nm, and total iron concentration was calculated from the standard curve.

Results

Immune-inflammatory activation and TFR1 enrichment on LDs in BAT

Principal component analysis (PCA) revealed that tissue type was the dominant source of variation, with the GS environment inducing secondary shifts within BAT and liver (Fig. S1). Transcriptomic analysis identified 400 upregulated and 260 downregulated genes in BAT under GS conditions (Fig. 1Aa). Focusing on metabolism and immunity (derived from Fig. S2), KEGG enrichment showed that these differentially expressed genes were primarily associated with immune-inflammatory pathways and lipid metabolism (Fig. 1Ab, Table S2). Similarly, LD proteomics identified 36 upregulated and 25 downregulated proteins (Fig. 1Ba). KEGG enrichment of the proteome revealed pathways related to the phagosome and lipid metabolism (Fig. 1Bb, Table S3).

Integration of transcriptomic and LD proteomic data via Sankey analysis linked these changes to glycerolipid metabolism, specifically showing the upregulation of 1-acylglycerol-3-phosphate O-acyltransferase 1/2 (AGPAT1/2) and aldehyde dehydrogenase 3 family member B2 (ALDH3B2) at the LD proteome level (Fig. 2A). Moreover, TFR1 and ALDH3B2 were significantly increased at both transcriptional and LD protein levels (Fig. 2B). qPCR validation confirmed the upregulation of C-C motif chemokine ligand 2 (*CCL2*) and C-X-C motif chemokine ligand 1 (*CXCL1*) in the GS group (Fig. 2C). Western blot analysis further revealed the enrichment of TFR1 and ATGL in the LD fractions (Fig. 2Da). Notably, TFR1 was highly enriched on LDs compared to other subcellular fractions in GS groups (Fig. 2Db).

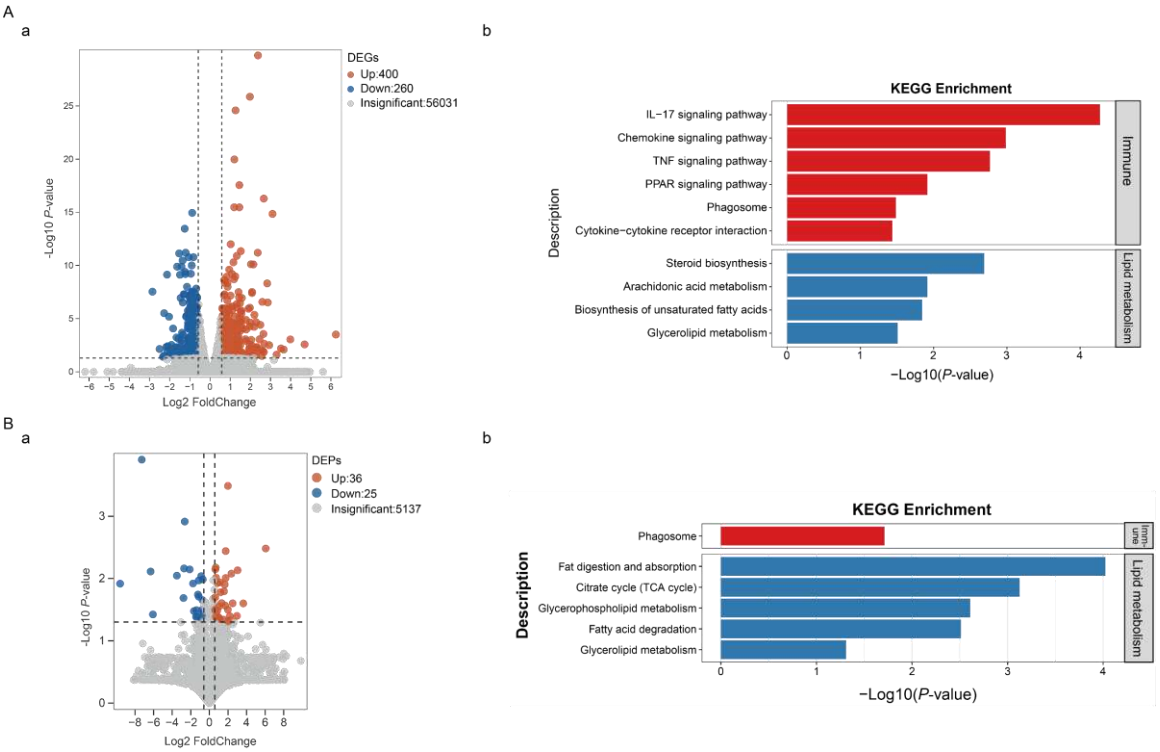


Fig. 1 Transcriptomic and LD proteomic analyses of BAT under geomagnetic field shielding. (A) BAT transcriptome analysis: (a) volcano plot of differentially expressed genes; (b) KEGG enrichment analysis. (B) BAT LD proteome analysis: (a) volcano plot of differentially expressed proteins; (b) KEGG enrichment analysis.

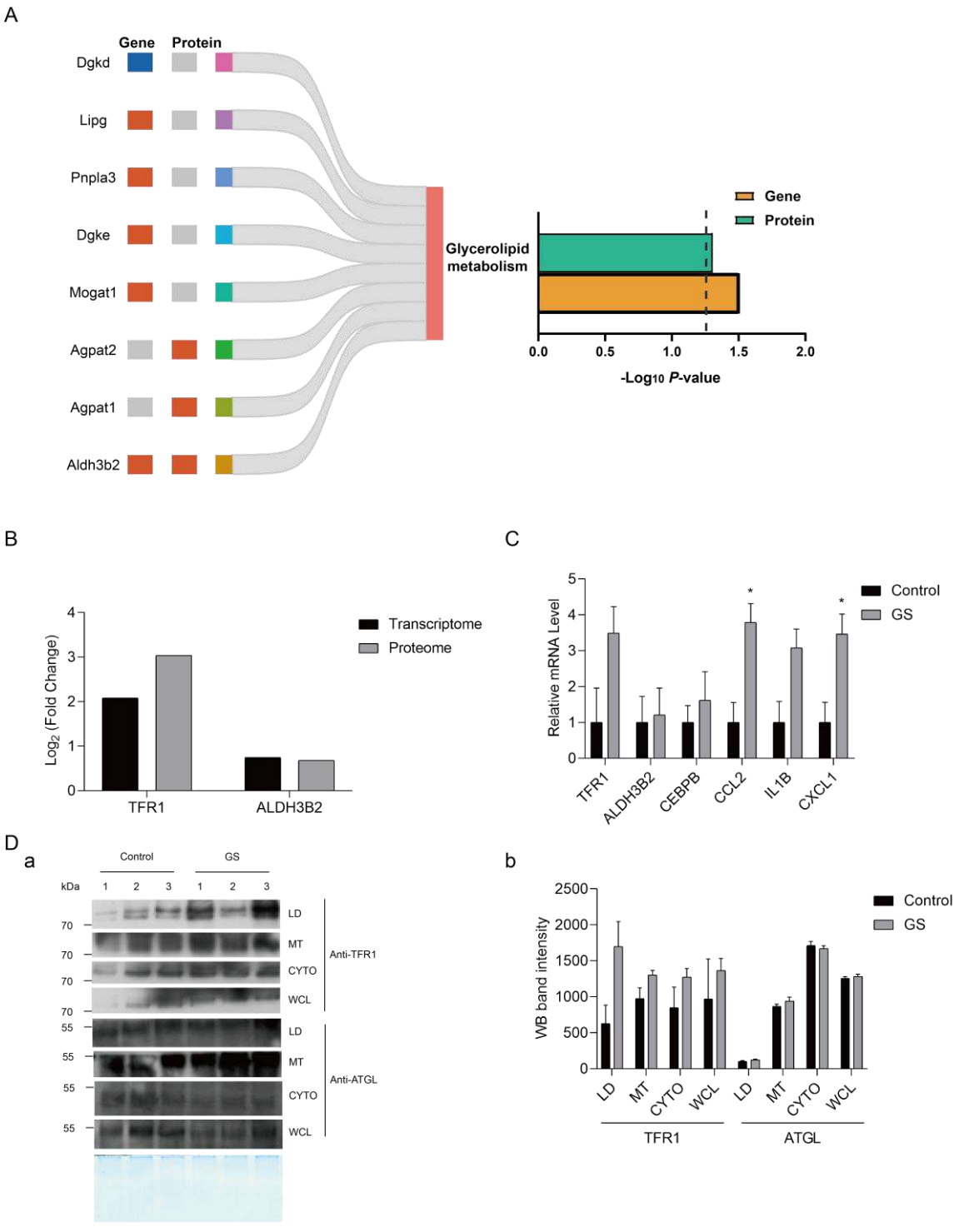


Fig. 2 Transcriptomic and LD proteomic profiling and validation of BAT under geomagnetic field shielding. (A) Sankey diagram of integrated BAT transcriptome and LD proteome analysis. Grey, red, and blue squares indicate non-significant, significantly upregulated, and significantly downregulated expression, respectively. All co-enriched pathways met P < 0.05 in both analyses. (B) Expression changes of TFR1 and ALDH3B2 in the transcriptome and LD proteome. Selected genes showed significant changes in both datasets; corresponding P-values are provided in Table S6. (C) qPCR validation of selected genes in BAT from GS and control mice. (D) Western blot analysis of BAT fractions. (a) Representative blots of TFR1 and ATGL in LD, MT, CYTO, and WCL fractions from GS and control mice. (b) ImageJ quantification of band intensities from (a). Data in (C) and (D, b) are presented as mean ± SEM (n = 3). $^{*}P < 0.05$ (unpaired t-test).

Hepatic lipid synthesis pathways are broadly enhanced

Unlike BAT, the liver exhibited a more pronounced response to the GS environment. Transcriptomic analysis identified 1,064 upregulated and 718 downregulated genes (Fig. 3Aa). Focusing on metabolism and immunity (derived from Fig. S3), KEGG enrichment showed that these genes were primarily involved in immune-related pathways and extensive lipid metabolic processes (Fig. 3Ab, Table S4). LD proteomics identified 127 upregulated and 127 downregulated proteins (Fig. 3Ba). KEGG enrichment of the proteome revealed pathways mainly enriched in antiviral/immune responses and broad lipid and energy metabolic pathways (Fig. 3Bb, Table S5).

Integrated Sankey analysis of the transcriptome and LD proteome revealed that cholesterol metabolism, fatty acid metabolism, and glycerophospholipid metabolism were the most prominently co-enriched pathways (Fig. 4A). Fifteen genes were significantly elevated at both transcriptomic and LD proteomic levels (Fig. 4B), including lipid synthesis regulators and antiviral defense-related proteins. qPCR validation showed an upward trend for diphosphomevalonate decarboxylase (*MVD*), thyroid hormone responsive (*THRSP*) and peroxisome proliferator-activated receptor delta (*PPARD*) (Fig. 4C). Western blot analysis of liver subcellular fractions showed that ATGL was present in the LD, CYTO, and WCL fractions, but was barely detectable in the TM fraction in both groups (Fig. 4Da-b). Quantitative analysis revealed that compared with the control, ATGL levels in the LD and CYTO fractions did not change significantly under GS conditions. In contrast, FASN levels were significantly decreased in the TM fraction, while its levels in the WCL fraction remained unchanged (Fig. 4Dc-d).

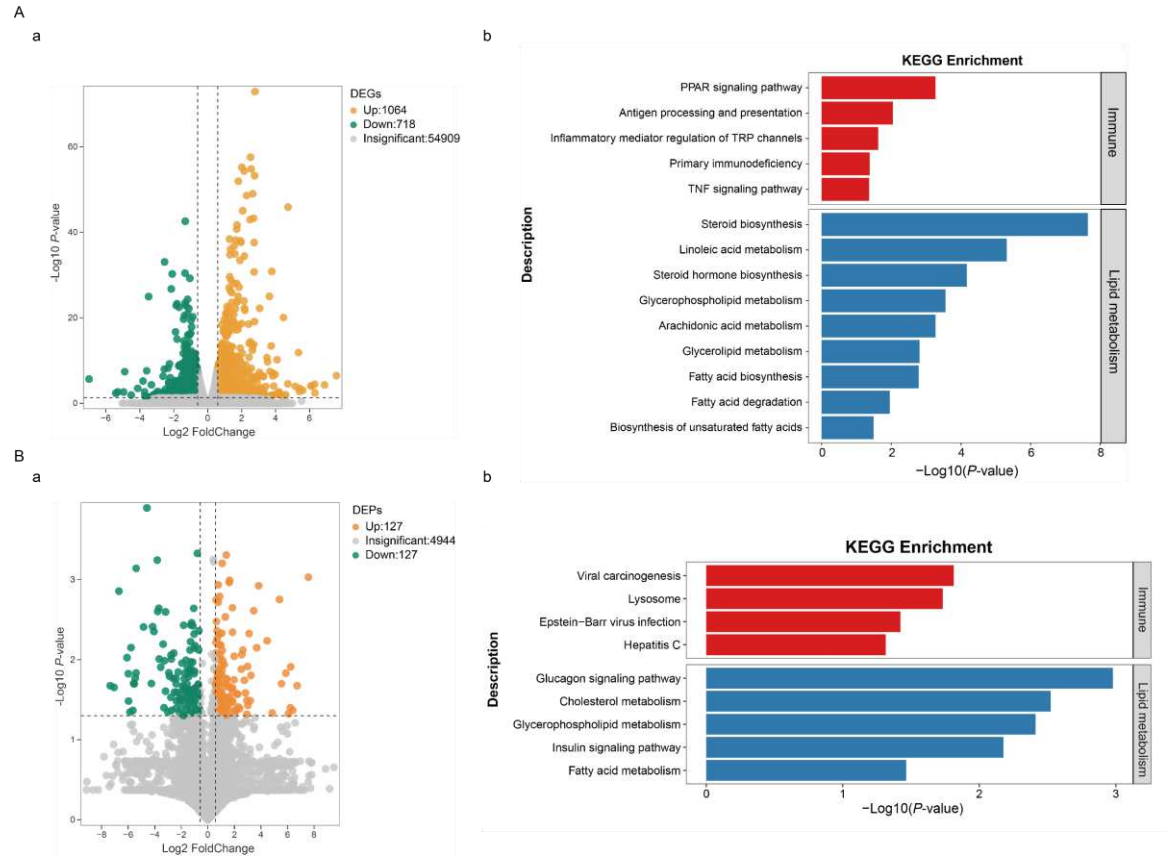


Fig. 3 Transcriptomic and LD proteomic analyses of liver under geomagnetic field shielding. (A) Liver transcriptome analysis: (a) volcano plot of differentially expressed genes; (b) KEGG enrichment analysis. (B) Liver LD proteome analysis: (a) volcano plot of differentially expressed proteins; (b) KEGG enrichment analysis.

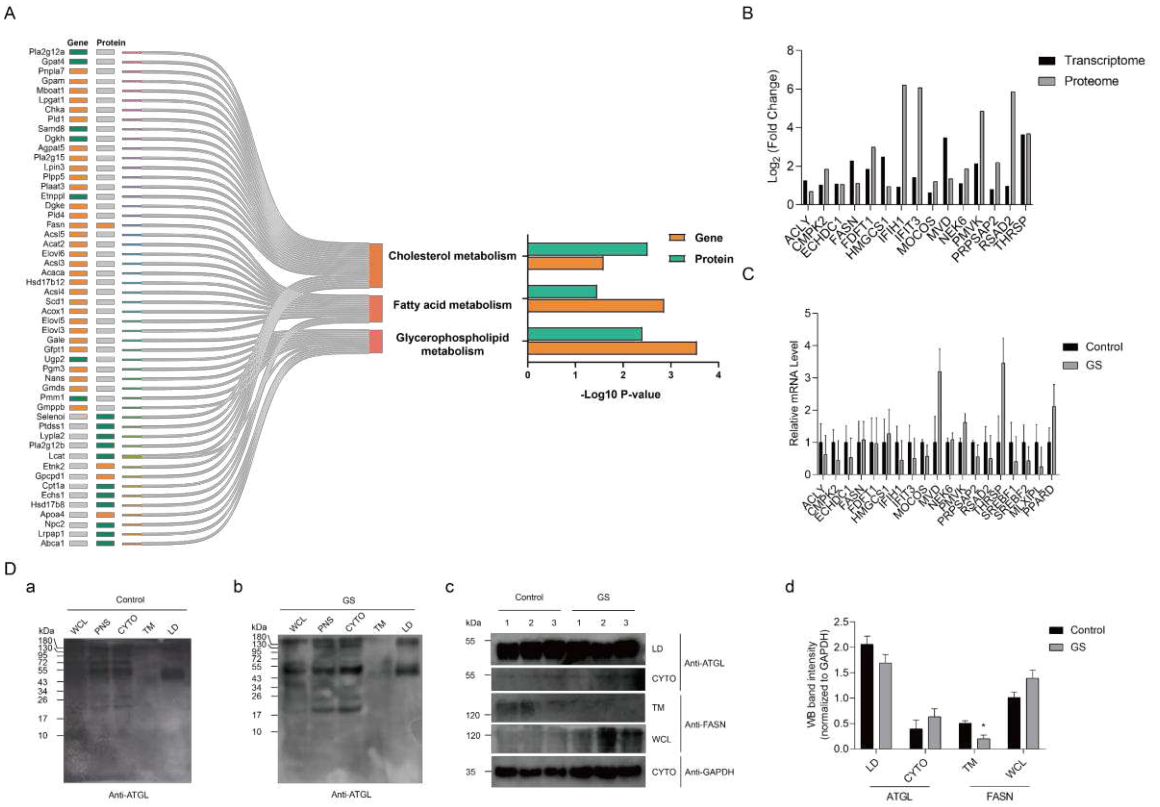


Fig. 4 Integrated transcriptomic and LD proteomic analyses of liver under geomagnetic field shielding with qPCR and Western blot validation. (A) Sankey diagram of integrated liver transcriptome and LD proteome analysis. Grey, orange, and green squares indicate non-significant, significantly upregulated, and significantly downregulated expression, respectively. All co-enriched pathways met $P < 0.05$ in both analyses. (B) Bar chart showing expression changes of 15 genes under geomagnetic field shielding. Statistical support is detailed in Table S6. (C) qPCR validation of selected genes in liver from GS and control mice. (D) Western blot analysis of liver fractions. (a) Representative blot of ATGL in WCL, PNS, CYTO, TM, and LD fractions from control mice. (b) Representative blot of ATGL in WCL, PNS, CYTO, TM, and LD fractions from GS mice. (c) Representative blots of ATGL in LD and CYTO fractions, FASN in TM and WCL fractions, and GAPDH in CYTO fractions from GS and control mice. (d) ImageJ quantification of band intensities from (c) normalized to GAPDH. Data in (C) and (D, d) are presented as mean ± SEM (n = 3). $^{*}P < 0.05$ (unpaired t-test).

Lipid composition and iron levels in isolated LDs

Silver staining of purified LDs from BAT and liver revealed faint bands, indicating low protein yield and confirming the necessity of using sensitive micro-proteomic approaches (Fig. S4A). Quantification of cytosolic total iron showed no statistically significant differences between the control and GS groups in either BAT or liver (Fig. S4B-C).

To determine whether the transcriptomic and proteomic changes manifest as actual lipid alterations, the lipid composition of isolated LDs was analyzed. TLC of LDs from BAT (Fig. 5Aa) and liver (Fig. 5Ab), along with subsequent densitometric quantification (Fig. 5B), revealed no significant differences in the relative PC content between the control and GS groups in either tissue. However, quantitative analysis of TAG revealed a significant increase in hepatic LDs from the GS group compared to the control group. In contrast, the TAG content in BAT LDs remained unchanged (Fig. 5C). These results suggest that the GS environment specifically promotes hepatic TAG accumulation.

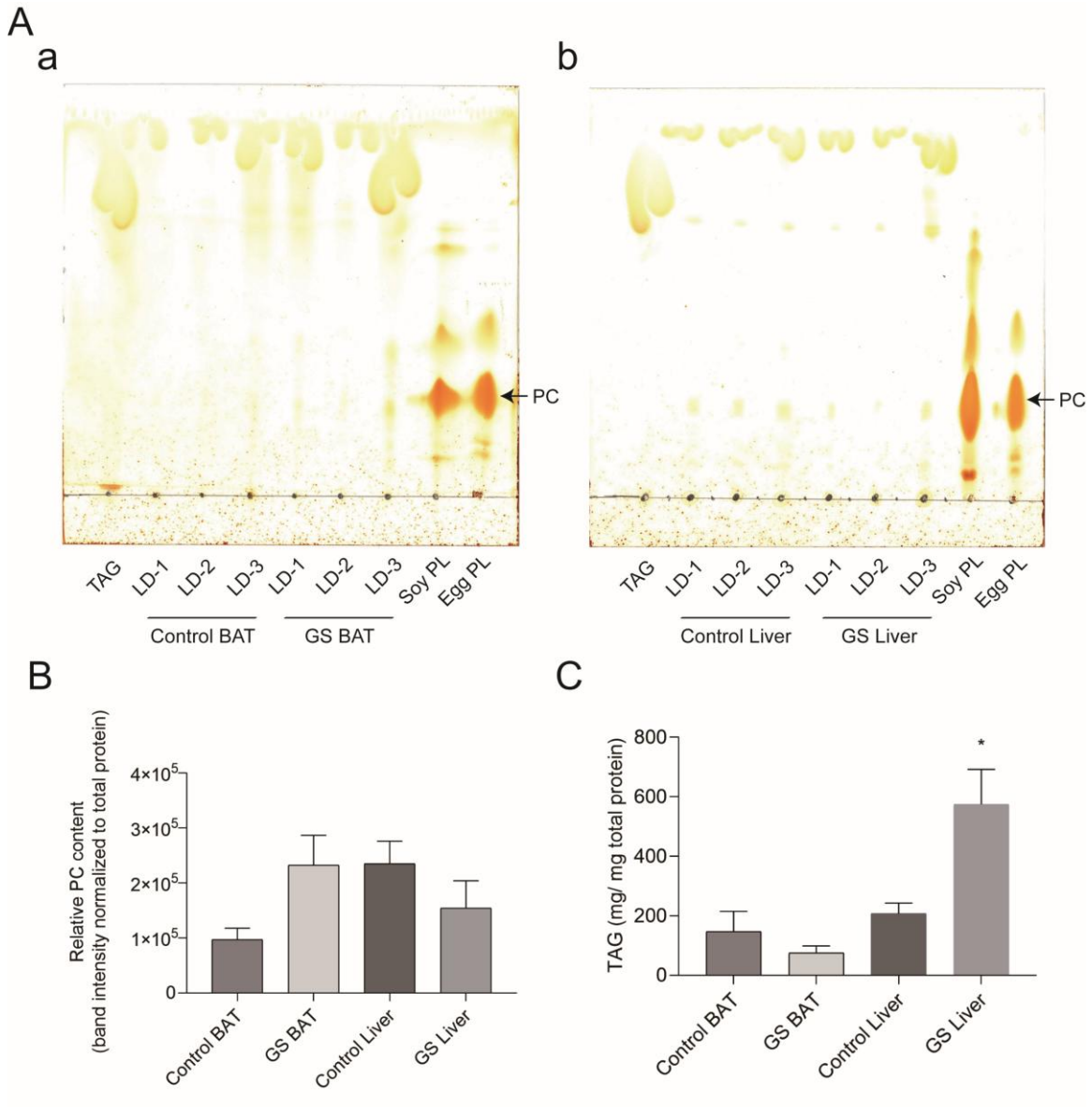


Fig. 5 Effects of geomagnetic field shielding on the lipid composition of LDs from BAT and liver. (A) TLC analysis of lipids from BAT (a) and liver (b) LDs. Lanes: 1, TAG marker (triolein); 2-4, control BAT LDs (biological replicates, n = 3); 5-7, GS BAT LDs (n = 3); 8, egg phospholipid (primarily phosphatidylcholine, PC) marker; 9, soy phospholipid (primarily PC) marker. Lane arrangement in (b) is identical to (a). (B) Densitometric quantification of PC bands normalized to total protein from TLC plates in (A), analyzed using ImageJ. (C) Quantitative analysis of TAG content in purified LDs from BAT and liver using an Amplex Red assay kit. TAG amount was normalized to LD protein content. Data in (B) and (C) are presented as mean ± SEM (n = 3). $^{*}P < 0.05$ (unpaired t-test).

Novel lncRNAs in BAT and liver under GS

To study the regulatory mechanisms of gene expression under GS, novel lncRNAs were identified in BAT and liver (Tables S7-8). Based on their host genes, these lncRNAs were divided into several functional categories. Some antisense lncRNAs overlapped with genes related to lipid metabolism and LD function, such as Fasn-201, Thrsp-201, and diacylglycerol O-acyltransferase 2 (Dgat2)-201 in the liver, and perilipin 4 (Plin4)-201 and cell death-inducing DFFA-like effector c (Cidec)-202 in BAT. Others overlapped with genes involved in immune and inflammatory responses, such as CCAAT/enhancer-binding protein beta (Cebpb)-201, Lysozyme 2 (Lyz2)-201, and macrophage scavenger receptor 1 (Msr1)-202. Additionally, some lncRNAs, such as succinate dehydrogenase complex subunit A (Sdha)-201 and succinate dehydrogenase complex subunit C (Sdhc)-202, were linked to mitochondrial energy metabolism, while period circadian regulator 2 (Per2)-201 was associated with the circadian gene Per2. The overlap of these lncRNAs with key metabolic and immune genes suggests that they might play a role in regulating host gene expression under GS.

Discussion

This study shows that GS environment causes different immune-metabolic changes in different tissues. In BAT, GS environment was linked to immune inflammation activation and metabolism changes related to LDs. In liver, GS environment was associated with activated lipid metabolism and innate immune responses. Although the two tissues responded differently to GS environment, both responses were closely related to LDs - TFR1 was enriched on LDs in BAT, and TAG accumulated in liver LDs. This suggests that LDs might act as a hub for the crosstalk between immunity and metabolism, mediating tissue-specific adaptations to GS environment(28).

In BAT, GS environment was found related to the activation of immune-inflammatory pathways. The enrichment of transcription factors like Cebpb and Fos, alert proteins like S100a8 and S100a9, and chemokines like Ccl2 and Cxcl1 suggests increased inflammation and immune cell recruitment (Table S2). Previous studies have shown that LDs accumulated in immune cells in response to stimuli to regulate the local inflammatory microenvironment(29). Therefore, in this study, BAT LDs were isolated and purified, LD proteins were detected and analyzed through proteomics, as well as verified via Western blot, and TFR1 was found enriched on BAT LDs. TFR1 is a protein involved in iron uptake. In order to explore its role on LDs, total iron in cytosol was measured. However, there was no significant change between the GS and control group, which indicates that TFR1 recruited to LDs mainly mediates iron transport to LD surface, probably supporting iron-dependent lipid metabolism related enzymes(30-32). Besides, studies have reported that TFR1 and iron metabolism regulation were involved in magnetic field-induced osteocyte differentiation(11, 33), suggesting that iron transportation to LDs by TFR1 might be conserved across different tissues. However, although iron is indispensable to certain enzymes on LDs, excess local iron may trigger ferroptosis by catalyzing lipid peroxidation(30, 32). In addition to TFR1, ALDH3B2 was also found increased under GS environment in both transcriptome and LD proteome, playing part in antioxidant defense. The enrichment of TFR1 and ALDH3B2 on BAT LDs in GS group suggests that LDs play a key role in dynamically balancing peroxidation and antioxidation, which is supported by other research. For example, iron overload affected LD formation in liver through heme oxygenase-1-mediated ferroptosis pathways(32). Conversely, LD accumulation acted as a protective mechanism to resist ferroptosis(34). Therefore, under GS conditions, balance between antioxidation and peroxidation on LD surface may determine whether brown adipocytes undergo ferroptosis due to lipid peroxidation(34, 35). Additionally, Per2-related novel antisense lncRNA indicates that GS environment may also affect the circadian rhythm of BAT(36), which requires further investigation.

In liver, GS environment was associated with broad activation of lipid metabolism, with cholesterol, fatty acid, and glycerophospholipid metabolic pathways enriched in the integrated analysis of the transcriptome and LD proteome. Furthermore, isolation and purification of liver LDs and TAG measurement revealed that TAG in LDs significantly increased under GS environment, indicating that GS might lead to lipid accumulation. This is consistent with previous findings that low magnetic field environments can alter liver lipid homeostasis(17). Since TAG accumulation is regulated by both lipid synthesis and lipolysis, expression and localization of ATGL, one of the key lipases on LDs, were examined. Although it was shown that expression and localization of ATGL on LDs remained unchanged, alterations of its enzymatic activity might be another reason for TAG increase. Given that ATGL activity is modulated by phosphorylation and co-activators(37-40), it requires further verification whether alteration of ATGL activity led to TAG accumulation in liver LDs. Regarding lipid synthesis, it was found that FASN, related to lipid synthesis, was significantly upregulated at both transcriptomic and LD proteomic levels. Subsequent Western blot analysis showed that FASN in WCL remained unchanged, but it was significantly reduced in the TM fraction. This suggests that TAG accumulation is not caused by increased FASN expression, but its subcellular redistribution (e.g., from the total membrane to the cytosol or LDs) to promote TAG synthesis(41). Meanwhile, the upregulation of interferon-stimulated genes in liver indicates innate immune activation, and enrichment of pathways such as virus-induced carcinogenesis and hepatitis C infection suggests a virus-like stress response in liver under GS conditions(42, 43). As previous studies demonstrated, inflammatory signals induced lipogenesis via liver X receptor (LXR)-dependent pathways(44). Therefore, the immune activation observed might act as an upstream factor for TAG accumulation in LDs(45). Additionally, novel lncRNAs found in liver under GS conditions may be involved in the transcriptional or post-transcriptional regulation of these immune and metabolic genes.

In addition, GS could affect lipid metabolism and redox processes in different species. For example, it was reported that the expression of genes related to lipids and reactive oxygen in plants(46), and mitochondrial respiration in fruit flies (15) were both affected by HMF. The conserved responses across

different species suggest that magnetic fields can regulate cellular energy metabolism and stress adaptability.

Overall, these results demonstrated that under GS environment, BAT was mainly associated with immune inflammation and TFR1 enrichment on LD, while liver was related to enhanced lipid metabolism and innate immune responses. Distinct responses may be the result of different physiological functions: BAT is a thermogenic and endocrine organ, whereas liver is mainly responsible for lipid metabolism. Moreover, Novel lncRNAs provides clues for understanding transcriptional and post-transcriptional regulation in BAT and liver under GS conditions. These findings highlight the tissue-specific effects of GS environment and provide a reference for health protection strategies in deep-space missions.

Limitations

There are several limitations in this study. First, residual magnetic field in GS environment was estimated by previous experience, which was reliable but not accurate. Second, small sample size (n = 3) resulted in large standard error of values, making it difficult to determine whether the difference is significant. Third, Inflammatory protein levels and immune cell infiltration in BAT, tissue lipid deposition, serum TAG and liver function in liver were not detected due to limitations of experimental conditions. Fourth, since body weight, food and water intake, stress behaviors, and blood parameters were not assessed, pathological impact of GS environment is still unclear. Finally, the function of TFR1 on LDs and novel lncRNAs haven't been verified.

Abbreviations

ACTB	Actin beta
AGPAT1/2	1-acylglycerol-3-phosphate O-acyltransferase 1/2
ALDH3B2	Aldehyde dehydrogenase 3 family member B2
ATGL	Adipose triglyceride lipase
BAT	Brown adipose tissue
BCA	Bicinchoninic acid assay
C. elegans	*Caenorhabditis elegans*
CCL2	C-C motif chemokine ligand 2
cDNA	Complementary DNA
Cebpb	CCAAT/enhancer-binding protein beta
Cidec	Cell death-inducing DFFA-like effector c
CPC	Coding potential calculator
CXCL1	C-X-C motif chemokine ligand 1
CYTO	Cytosol
DGAT2	Diacylglycerol O-acyltransferase 2
DIA	Data-independent acquisition
FASN	Fatty acid synthase
FDR	False discovery rate
GAPDH	Glyceraldehyde-3-phosphate dehydrogenase
GMF	Geomagnetic field
GS	Geomagnetic shielding
GSK-3β	Glycogen synthase kinase-3 beta
HEPES	4-(2-hydroxyethyl)-1-piperazineethanesulfonic acid
HMF	Hypomagnetic field
HRP	Horseradish peroxidase
IFN-γ	Interferon-gamma
IL-18R1	Interleukin-18 receptor 1
KEGG	Kyoto Encyclopedia of Genes and Genomes
LD	Lipid droplet
lncRNA	Long non-coding RNA
log2FC	Log2 fold change
LXR	Liver X receptor
Lyz2	Lysozyme 2

Msr1 Macrophage scavenger receptor 1
miRNA MicroRNA
MT Mitochondria
mTOR Mammalian target of rapamycin
MVD Diphosphomevalonate decarboxylase
NADPH Nicotinamide adenine dinucleotide phosphate
NO Nitric oxide
PBS Phosphate-buffered saline
PC Phosphatidylcholine
PCA Principal component analysis
Per2 Period circadian regulator 2
Plin4 Perilipin 4
PNS Post-nuclear supernatant
PPARD Peroxisome proliferator-activated receptor delta
PVDF Polyvinylidene fluoride
qPCR Quantitative polymerase chain reaction
rRNA Ribosomal RNA
ROS Reactive oxygen species
Sdha Succinate dehydrogenase complex subunit A
Sdhc Succinate dehydrogenase complex subunit C
SDS-PAGE Sodium dodecyl sulfate-polyacrylamide gel electrophoresis
snoRNA Small nucleolar RNA
TAG Triacylglycerol
TBST Tris-buffered saline with Tween 20
TFR1 Transferrin receptor 1
THRSP Thyroid hormone-inducible hepatic protein
TLC Thin-layer chromatography
TM Total membrane
Treg Regulatory T cell
tRNA Transfer RNA
WCL Whole-cell lysate

Supplementary Information

Figures
Fig. S1 PCA of the transcriptome and LD proteome in BAT and liver.
Fig. S2 Transcriptomic and LD proteomic analyses of BAT under GS conditions.
Fig. S3 Transcriptomic and LD proteomic analyses of liver under GS conditions.
Fig. S4 Analysis of LD protein yield and total iron in BAT and liver cytosol.
Fig. S5 Hourly variation range of the ambient GMF during the experimental period.

Tables
Table S1 Primers used for qPCR.
Table S2 KEGG pathways and enriched genes in BAT (Control vs GS).
Table S3 KEGG pathways and enriched proteins in BAT (Control vs GS).
Table S4 KEGG pathways and enriched genes in liver (Control vs GS).
Table S5 KEGG pathways and enriched proteins in liver (Control vs GS).
Table S6 Genes significantly up-regulated in both transcriptome and LD proteome.
Table S7 Novel lncRNAs identified in BAT (Control vs GS).
Table S8 Novel lncRNAs identified in liver (Control vs GS).

Declarations

Ethics approval and consent to participate

All experimental procedures involving animals were approved by the Animal Ethical and Welfare

Committee of Cell Ecology Haihe Laboratory (Approval No: HH-DWLL-YW2025009-1).

Consent for publication

Not applicable.

Availability of data and materials

The datasets supporting the findings of this study are included in the article and its supplementary files. The raw transcriptome sequencing data have been deposited in the CNGB Sequence Archive (CNSA) of China National Center for Bioinformation (CNCB) under accession number PRJCA052161. The mass spectrometry proteomics data have been deposited to the ProteomeXchange Consortium (https://proteomecentral.proteomexchange.org) via the iProX partner repository with the dataset identifier PXD076066.

Competing interests

The authors declare no competing interests.

Funding

This work was supported by the grant from Cangzhou Natural Science Foundation (221001002D).

Authors' contributions

XM conceived and designed the study. XM acquired the funding, performed the experiments, analyzed the data, and drafted the manuscript. DG handled the mice and performed the experiments. GK analyzed the data. WX contributed to manuscript writing. JXZ, HLW, SYD, JYZ, RXZ and XYJ assisted with the experiments. All authors read and approved the final manuscript.

Acknowledgements

The authors thank Associate Investigator ZHANG Bing-Fang (Institute of Biomedical Engineering, Chinese Academy of Medical Sciences & Peking Union Medical College) for providing the mice and establishing the GS mouse model, as well as for her valuable input during data analysis and manuscript preparation. The authors would like to express their sincere gratitude to Mr. Jianbo Liu from the Tianjin Earthquake Agency for his valuable assistance in estimating the local geomagnetic field intensity in the Tianjin region.

References

1. Tarduno JA, Cottrell RD, Watkeys MK, Hofmann A, Doubrovine PV, Mamajek EE, et al. Geodynamo, Solar Wind, and Magnetopause 3.4 to 3.45 Billion Years Ago. Science. 2010;327(5970):1238-40.
2. Erdmann W, Idzikowski B, Kowalski W, Kosicki JZ, Kaczmarek Ł. Tolerance of two anhydrobiotic tardigrades Echiniscus testudo and Milnesium inceptum to hypomagnetic conditions. PeerJ. 2021;9:e10630.
3. Kokhan VS, Matveeva MI, Mukhametov A, Shtemberg AS. Risk of defeats in the central nervous system during deep space missions. Neuroscience & Biobehavioral Reviews. 2016;71:621-32.
4. Mo WC, Hu PD, Fan Z, Liu Y, He RQ. The biochemical and molecular mechanisms underlying the effects of the hypomagnetic field in animals. Chemistry of Life. 2019;39(5):930-5
5. Zhang B, Tian L. Reactive Oxygen Species: Potential Regulatory Molecules in Response to Hypomagnetic Field Exposure. Bioelectromagnetics. 2020;41(8):573-80.

6. Baek S, Choi H, Park H, Cho B, Kim S, Kim J. Effects of a hypomagnetic field on DNA methylation during the differentiation of embryonic stem cells. Sci Rep. 2019;9(1):1333.
7. Dang N, Keller J, Barnes F. Biological impacts of hypomagnetic fields in space environment: implications for artificial magnetic field provision in long-duration spaceflight. Frontiers in Space Technologies. 2025; 6:1704391.
8. Tian L, Luo Y, Ren J, Zhao C. The Role of Oxidative Stress in Hypomagnetic Field Effects. Antioxidants (Basel). 2024;13(8):1017.
9. Ren J, Li F, Shen J, Tian L, Pan Y. GSK-3β and mTOR Phosphorylation Mediate the Reversible Regulation of Hypomagnetic Field on Adult Neural Stem Cell Proliferation. Eur J Neurosci. 2025;62(2):e70202.
10. Yang J, Meng X, Dong D, Xue Y, Chen X, Wang S, et al. Iron overload involved in the enhancement of unloading-induced bone loss by hypomagnetic field. Bone. 2018;114:235-45.
11. Zhang G, Zhen C, Yang J, Zhang Z, Wu Y, Che J, et al. 1-2 T static magnetic field combined with Ferumoxytol prevent unloading-induced bone loss by regulating iron metabolism in osteoclastogenesis. Journal of Orthopaedic Translation. 2023;38:126-40.
12. Xue Y, Yang J, Luo J, Ren L, Shen Y, Dong D, et al. Disorder of Iron Metabolism Inhibits the Recovery of Unloading-Induced Bone Loss in Hypomagnetic Field. J Bone Miner Res. 2020;35(6):1163-73.
13. Tian L, Ren J, Luo Y. The effects of different durations of exposure to hypomagnetic field on the number of active mitochondria and ROS levels in the mouse hippocampus. Biochem Biophys Rep. 2024;38:101696.
14. Wang GM, Fu JP, Mo WC, Zhang HT, Liu Y, He RQ. Shielded geomagnetic field accelerates glucose consumption in human neuroblastoma cells by promoting anaerobic glycolysis. Biochem Biophys Res Commun. 2022;601:101-8.
15. Ogneva IV, Usik MA, Burtseva MV, Biryukov NS, Zhdankina YS, Sychev VN, et al. Drosophila melanogaster Sperm under Simulated Microgravity and a Hypomagnetic Field: Motility and Cell Respiration. Int J Mol Sci. 2020;21(17):5985.
16. Ping-Dong HU, Wei-Chuan MO, Jing-Peng FU, Ying LIU, Rong-Qiao HE. Long-term Hypogeomagnetic Field Exposure Reduces Muscular Mitochondrial Function and Exercise Capacity in Adult Male Mice. Progress in Biochemistry and Biophysics. 2020;47(5):426-38.
17. Babych VI. The characteristics of tissue lipid peroxidation in the internal organs and the lipid metabolic indices of the blood plasma in a low geomagnetic field. Fiziol Zh (1994). 1995;41(5-6):44-9.
18. Shust IV, Kostinik IM. Effect of a strong constant magnetic field and a hypomagnetic surrounding medium on histochemical indices of albino rat liver. Kosm Biol Aviakosm Med. 1975;9(6):19-25.
19. Roman A, Tombarkiewicz B. Prolonged weakening of the geomagnetic field (GMF) affects the immune system of rats. Bioelectromagnetics. 2009;30(1):21-8.
20. Montana A, Delaney P, Tetyana. The Effect of Hypomagnetic Field on C. elegans Development, Lifespan and Innate Immune Responses. The Journal of Immunology. 2024;212(1_Supplement):0630-4744.
21. Novikov VV, Yablokova EV, Shaev IA, Fesenko EE. Decreased Production of the Superoxide Anion Radical in Neutrophils Exposed to a Near-Null Magnetic Field. Biophysics. 2020;65(4):625-30.
22. Zammit NW, Vargas-Castillo A, Langston PK, Wang G, Zhou Y, Spiegelman BM, et al. Regulatory T cells in brown adipose tissue safeguard thermogenesis by restraining interferon-γ-producing lymphocytes. Sci Immunol. 2025;10(109):eads0478.
23. Zhao J, Hu L, Gui W, Xiao L, Wang W, Xia J, et al. Hepatocyte TGF-β Signaling Inhibiting WAT Browning to Promote NAFLD and Obesity Is Associated With Let-7b-5p. Hepatol Commun.

2022;6(6):1301-21.
24. Lee E, Korf H, Vidal-Puig A. An adipocentric perspective on the development and progression of non-alcoholic fatty liver disease. Journal of Hepatology. 2023;78(5):1048-62.
25. Zhang B, Wang L, Zhan A, Wang M, Tian L, Guo W, et al. Long-term exposure to a hypomagnetic field attenuates adult hippocampal neurogenesis and cognition. Nat Commun. 2021;12(1):1174.
26. Su W, Wang Y, Jia X, Wu W, Li L, Tian X, et al. Comparative proteomic study reveals 17β-HSD13 as a pathogenic protein in nonalcoholic fatty liver disease. Proceedings of the National Academy of Sciences. 2014;111(31):11437-42.
27. Cui L, Mirza AH, Zhang S, Liang B, Liu P. Lipid droplets and mitochondria are anchored during brown adipocyte differentiation. Protein Cell. 2021;12(9):746.
28. Yang J, Wang D, Dong X, Huo H, Tao R, Zhang Y, et al. Interaction Between Microglial Lipid Droplet Metabolism and Immune Polarisation After Stroke: Mechanisms and Therapeutic Prospects. Cell Mol Neurobiol. 2025;46(1):10.
29. Zhang S, Feng Y, Wu X, Chen J, Zhang H, Tian L, et al. IFN-γ induced the formation of foamy macrophages via CD40 signal to control Mycobacterium abscessus pulmonary infection. Front Immunol. 2025;16:1697443.
30. Pham LBH, Kim T, Kim S, Kim YS, Kim J, Kim K, et al. Novel Near-Infrared Probe for Monitoring Lipid Peroxidation-Mediated Viscosity Change in Ferroptotic Hepatocytes. Clin Mol Hepatol. 2026;32(1):318-338.
31. Wang H, Jiang X, Wu J, Zhang L, Huang J, Zhang Y, et al. Iron Overload Coordinately Promotes Ferritin Expression and Fat Accumulation in Caenorhabditis elegans. Genetics. 2016;203(1):241-53.
32. Ma W, Jia L, Zhao J, Li Y, Kong J, Du H. Iron regulates lipid droplet formation in hepatocytes via heme oxygenase-1 mediated ferroptosis. J Trace Elem Med Biol. 2025;91:127719.
33. Yang J, Zhang J, Ding C, Dong D, Shang P. Regulation of Osteoblast Differentiation and Iron Content in MC3T3-E1 Cells by Static Magnetic Field with Different Intensities. Biological Trace Element Research. 2018;184(1):214-25.
34. Chauhan SS, Vizzerra AD, Liou H, Flores CE, Snider AJ, Snider JM, et al. Hypoxia induced lipid droplet accumulation promotes resistance to ferroptosis in prostate cancer. Oncotarget. 2025;16:532-44.
35. Girotti AW, Korytowski W. Cholesterol Hydroperoxide Generation, Translocation, and Reductive Turnover in Biological Systems. Cell Biochemistry and Biophysics. 2017;75(3):413-9.
36. Zhang Y, Zeng L, Wei Y, Zhang M, Pan W, Sword GA, et al. Reliable reference genes for gene expression analyses under the hypomagnetic field in a migratory insect. Front Physiol. 2022;13:954228.
37. Kim SJ, Tang T, Abbott M, Viscarra JA, Wang Y, Sul HS. AMPK Phosphorylates Desnutrin/ATGL and Hormone-Sensitive Lipase To Regulate Lipolysis and Fatty Acid Oxidation within Adipose Tissue. Mol Cell Biol. 2016;36(14):1961-76.
38. Yang X, Lu X, Lombès M, Rha GB, Chi YI, Guerin TM, et al. The G(0)/G(1) switch gene 2 regulates adipose lipolysis through association with adipose triglyceride lipase. Cell Metab. 2010;11(3):194-205.
39. Lass A, Zimmermann R, Haemmerle G, Riederer M, Schoiswohl G, Schweiger M, et al. Adipose triglyceride lipase-mediated lipolysis of cellular fat stores is activated by CGI-58 and defective in Chanarin-Dorfman Syndrome. Cell Metab. 2006;3(5):309-19.
40. Xie X, Langlais P, Zhang X, Heckmann BL, Saarinen AM, Mandarino LJ, et al. Identification of a novel phosphorylation site in adipose triglyceride lipase as a regulator of lipid droplet localization. Am J Physiol Endocrinol Metab. 2014;306(12):E1449-59.
41. Wu Y, Shen J, Gao S, Li M, Weng Q, Zheng K, et al. Fatty acid synthase-mediated lipid droplet formation enhances macrophage killing of Staphylococcus aureus. Cell Death Dis. 2025;16(1):715.

42. Li X, Zhang H, Yu F, Xie S, Wang T, Zhang R, et al. IRF8 aggravates nonalcoholic fatty liver disease via BMAL1/PPARγ axis. Genes Dis. 2025;12(3):101333.
43. Weiss U, Mungo E, Haß M, Benning D, Gurke R, Hahnefeld L, et al. Knock-Out of IKKepsilon Ameliorates Atherosclerosis and Fatty Liver Disease by Alterations of Lipid Metabolism in the PCSK9 Model in Mice. Int J Mol Sci. 2024;25(19):10721.
44. Liebergall SR, Angdisen J, Chan SH, Chang Y, Osborne TF, Koeppel AF, et al. Inflammation Triggers Liver X Receptor-Dependent Lipogenesis. Mol Cell Biol. 2020;40(2):e00364-19.
45. Tong J, Han CJ, Zhang JZ, He WZ, Zhao GJ, Cheng X, et al. Hepatic Interferon Regulatory Factor 6 Alleviates Liver Steatosis and Metabolic Disorder by Transcriptionally Suppressing Peroxisome Proliferator-Activated Receptor γ in Mice. Hepatology. 2019;69(6):2471-88.
46. Mannino G, Parmagnani AS, Maffei ME. Reduction of the geomagnetic field to hypomagnetic field modulates tomato (Solanum lycopersicum L. cv Microtom) gene expression and metabolomics during plant development. J Plant Physiol. 2025;306:154453.

Supplementary Files

This is a list of supplementary files associated with this preprint. Click to download.

- SupplementarydataFigureS5.docx
- SupplementarydataFigureS2S3.docx
- SupplementarydataFigureS1.docx
- SupplementarydataFigureS4.docx
- SupplementarydataTableS1S6.docx
- SupplementarydataTableS1S6.docx
- SupplementarydataTableS7S8.docx
- SupplementarydataFigureS2S3.docx